

PAPER • OPEN ACCESS

Carbon erosion/deposition on the divertor of W7-X during the operational period OP 1.2b

To cite this article: M. Mayer *et al* 2022 *Nucl. Fusion* **62** 126049

View the [article online](#) for updates and enhancements.

You may also like

- [Erosion of tungsten marker layers in W7-X](#)
M Mayer, M Balden, S Brezinsek et al.
- [Material erosion and deposition on the divertor of W7-X](#)
M Mayer, M Balden, S Brezinsek et al.
- [Plasma–surface interaction in the stellarator W7-X: conclusions drawn from operation with graphite plasma-facing components](#)
S. Breznsek, C.P. Dhard, M. Jakubowski et al.

Carbon erosion/deposition on the divertor of W7-X during the operational period OP 1.2b

M. Mayer^{1,*}, M. Balden¹, S. Brezinsek², V.V. Burwitz¹, C. Cupak³, C.P. Dhard⁴, S. Elgeti¹, M. Guitart Corominas¹, P. Hired¹, M. Kandler¹, D. Naujoks⁴, J.-H. Schmidt-Dencker¹, C. Ruset⁵, T.B. Saramela⁶, T.F. Silva⁶ and the W7-X Team^a

¹ Max-Planck-Institut für Plasmaphysik, Garching, Germany

² Forschungszentrum Jülich GmbH, Jülich, Germany

³ Institute of Applied Physics, TU Wien, Vienna, Austria

⁴ Max-Planck-Institut für Plasmaphysik, Greifswald, Germany

⁵ National Institute for Laser, Plasma and Radiation Physics, Bucharest, Romania

⁶ University of São Paulo, São Paulo, Brazil

E-mail: matej.mayer@ipp.mpg.de

Received 19 July 2022, revised 2 September 2022

Accepted for publication 26 September 2022

Published 31 October 2022



CrossMark

Abstract

Carbon net erosion and deposition at the test divertor unit (TDU) of Wendelstein 7-X (W7-X) were measured for the discharge period OP 1.2b in the year 2018 using 18 specially prepared target elements in all 10 TDUs. These had lengths between 30 and 60 cm and were coated with marker layers for erosion/deposition investigations of 5–10 μm carbon on top of about 300 nm molybdenum. The marker layer thicknesses were measured by elastic backscattering spectrometry (EBS) before and after plasma exposure using 2.5 MeV protons; the surface morphology was investigated using scanning electron microscopy (SEM) and focused ion beam cross-sectioning (FIB), the surface roughness was determined using a two-dimensional optical profiler. Plasma-exposed surfaces were considerably smoother than unexposed surfaces with decreased mean roughness and a shift of the inclination angle distribution towards lower values. The erosion on the 10 TDUs was unequal within a factor of about two. During the discharge period in total 20.4 ± 5.7 g carbon was eroded from the 10 TDUs. Adjacent to the strike line some deposition of carbon was observed. Compared to the discharge period OP 1.2a in the year 2017, the net carbon erosion rate dropped by a factor of 5–6 due to regular boronizations, which reduced the oxygen (and subsequently also the carbon) content in the plasma by 1–2 orders of magnitude. The significance of erosion/deposition processes for long-pulse discharges is discussed.

Keywords: W7-X, test divertor unit, TDU, erosion, divertor, ion beam analysis

(Some figures may appear in colour only in the online journal)

* Author to whom any correspondence should be addressed.

^a See Klinger *et al* 2019 (<https://doi.org/10.1088/1741-4326/ab03a7>) for the W7-X Team.

 Original content from this work may be used under the terms of the [Creative Commons Attribution 4.0 licence](https://creativecommons.org/licenses/by/4.0/). Any further distribution of this work must maintain attribution to the author(s) and the title of the work, journal citation and DOI.

1. Introduction

Wendelstein 7-X (W7-X), together with the Large Helical Device (LHD), is the world's largest stellarator with superconducting coils and a plasma volume of 30 m³ [1–4]. Plasma operation started in 2015, the second operational phase (OP 1.2) was performed in the years 2017 and 2018. Since OP 1.2 a divertor with adiabatic cooling, the test divertor unit (TDU), was used [5, 6]. This divertor was complemented by baffles, the inner wall was covered by the inner heat shield. Most PFCs (except for the outer vessel wall and pumping gap panels) consist of fine-grain graphite. The W7-X divertor uses the island divertor concept [7] with multiple magnetic islands at the plasma edge providing several x -points. This divertor concept was initially developed at the predecessor device W7-AS [8]. The TDU had the same shape towards the plasma as the current steady-state divertor with water-cooled PFCs made from carbon-fiber-composites, which was installed during the years 2019–2021 and will be in operation starting in the year 2022. This divertor should finally allow long-pulse discharges up to 1800 s.

Investigations of plasma–surface interactions (PSI) in W7-X are challenging due to the three-dimensional geometry, the bent shapes and large sizes of most PFCs, and the high heat loads at the divertor strike lines of up to 10 MW m⁻². Despite these difficulties OP 1.2 offered the unique possibility to study PSI phenomena in W7-X in some detail using surface-analytical techniques due to the passive cooling. This will be no longer possible in OP 2 and beyond, where the requirement for water-cooled plasma-exposed surfaces severely limits the possibilities for sample exposure and exchange. For PSI investigations special exchangeable divertor target elements were developed and coated with C/Mo marker layers for erosion/deposition investigations. One set of elements was exposed in 2017 during the operational period OP 1.2a [9] and exchanged during the vessel opening between the operational phases OP 1.2a and OP 1.2b. The observed erosion/deposition pattern after OP 1.2a was already described in [9]. This paper describes the results observed in OP 1.2b.

During OP 1.2a only glow discharge cleaning was used for wall conditioning, while boronizations were not performed. In OP 1.2b, three boronizations were used, resulting in a substantial decrease of the oxygen and carbon concentrations in the plasma [10, 11]: after the third boronization the oxygen levels were about two orders of magnitude lower compared to the levels before the boronizations, while in reference discharges the value of Z_{eff} decreased from 4.5 to about 1.2. This decreased low- Z impurity concentration allowed the operational window of W7-X to be extended towards higher plasma densities by a factor of more than 2.5 and towards higher diamagnetic energies by a factor of about 1.5 [10, 12]. The decreased impurity content resulted also in a substantial change of the erosion/deposition behavior on the TDU, which is described in this paper. Erosion/deposition phenomena are also crucial for the envisaged long-pulse operation of W7-X with pulse-lengths up to 1800 s. The experimental

Table 1. Total plasma time and plasma time in standard configuration in OP 1.2a and OP 1.2b; carbon erosion on the horizontal and vertical TDU and the total (horizontal + vertical) carbon erosion on the TDU; carbon erosion rate on the horizontal and vertical TDU.

	OP 1.2a	OP 1.2b
Total plasma time (s)	3775	9054
Standard configuration plasma time (s)	2481	4809
Carbon erosion (g)		
Horizontal	34.5 ± 8.4	13.7 ± 2.3
Vertical	13.3 ± 5.7	6.7 ± 3.4
Total	47.8 ± 14.1	20.4 ± 5.7
Carbon erosion rate (mg s⁻¹)		
Horizontal	13.9 ± 3.4	2.3 ± 0.4
Vertical	4.2 ± 1.8	0.9 ± 0.5

observations in the already realized operational periods allow us to draw conclusions for the foreseen long-pulse operation.

2. Experimental

2.1. Plasma operation

The discharge period OP 1.2a was performed from August 2017 to December 2017 and consisted of 1248 plasma discharges with an integrated plasma time of 3776 s, see table 1. For details of different plasma configurations see [9, table 1 or 13, table 1]. The majority of discharges were in the so-called Standard configuration (with 65.7% of the plasma time). The residual discharges were in high mirror or high iota configuration, while there were no low iota discharges in OP 1.2a. With 72.2% of the plasma time most discharges were He-fueled. However, also these discharges were typically mixed H + He plasmas with a majority of H and often only minor He content. The hydrogen most probably originated from outgassing of trapped H from the vessel walls.

The discharge phase OP 1.2b took place from July to October 2018 and had a total plasma time of 9054 s, see table 1 or [13, table 2]. The majority of discharges with 53.1% of the plasma time (4809 s) were in standard configuration, the other discharges were in high iota (1673 s), low iota (1180 s), or high mirror (1392 s) configuration. These configurations have their strike lines on different parts of the TDU [6]. All plasma discharges were hydrogen fueled. While a large variation of plasmas was performed, the plasma time of more exotic configurations was limited. The dominant plasma scenario in OP 1.2b had an ECR heating power of 3–4 MW, a pulse length of about 10 s, and usually attached divertor conditions.

The strike line of the standard configuration is on vertical target modules TM1v to TM3v and horizontal target modules TM1h to TM4h, see figure 1 for a schematic representation of the modules. The strike line of the High Mirror configuration is on vertical modules TM1v to TM3v and horizontal

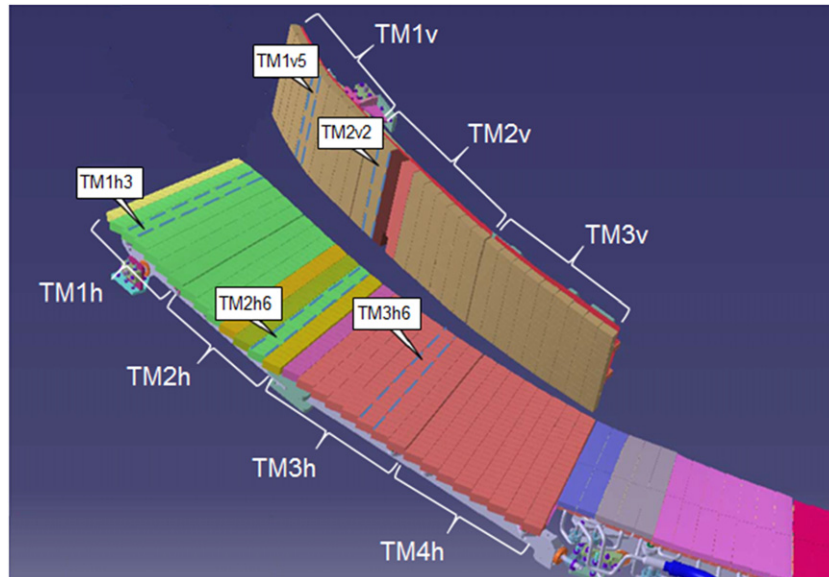


Figure 1. Schematic representation of the PSI target elements in the TDU. TM_{yv} are vertical target modules; TM_{xh} are horizontal target modules. TM_{xhz} is the z 'th element in target module x . Dashed lines indicate target elements with marker layers. The pumping gap is the gap between the horizontal and the vertical target. Reproduced from [9]. © 2020 The Royal Swedish Academy of Sciences. All rights reserved.

Table 2. Positions and applied analysis methods of PSI target elements in the TDU during the operational period OP 1.2b. A graphical representation of the positions is shown in figure 1. TDU 1l is the lower TDU in module 1, TDU 1u is the upper TDU in module 1 etc. TM_{xhy} elements are in the horizontal TDU, TM_{xvy} are in the vertical TDU. IBA: ion beam analysis; SEM: scanning electron microscopy; FIB: focused ion beam cross-sectioning; profilometer: optical profiler. PSI elements TM2h6 in TDU 1l was partly tungsten coated, see [43] for details.

TDU	PSI element	Analysis methods
1l	TM2h6 (W-coated)	IBA
1u	TM2h6	IBA
2l	TM2h6	IBA
2u	TM2h6	IBA, SEM, FIB, Profilometer
3l	TM2h6	IBA
3u	TM2h6	IBA
4l	TM2h6	IBA
4u	TM2h6	IBA
5l	TM1h3, TM2h6, TM3h6, TM1v5, TM2v2	IBA
5u	TM1h3, TM2h6, TM3h6, TM1v5, TM2v2	IBA

modules TM3h to TM4h, while the strike line of the High Iota configuration is in the high iota part of the divertor (which is beyond the area containing marker samples). See e.g. [6] for a graphical representation of the strike line positions of the different plasma configurations. The divertor heat load at the strike line was up to 8 MW m^{-2} , the strike line width was up to 11 cm. The plasma-wetted divertor area was a function of ECRH heating power and increased about linearly to values of about 1.5 m^2 at 5 MW [6]. The bulk temperature of divertor tiles increased seldomly up to $400 \text{ }^\circ\text{C}$ during the experimental day [6]. The strike line surface temperature sometimes reached temperatures close to $800 \text{ }^\circ\text{C}$ [14]. Typical electron temperatures were 50–100 eV in the scrape-off layer with electron densities in the range $2\text{--}6 \times 10^{18} \text{ m}^{-3}$ [15, 16].

While no boronizations were applied in OP 1.2a, three boronizations were applied in OP 1.2b [17]. As result of the

boronizations, thin boron layers (typically containing also carbon and oxygen) with thicknesses of a few 10 nm were found on all wall elements in W7-X [18].

2.2. PSI target elements

Erosion/deposition investigations in W7-X required the development of exchangeable PSI target elements [19], a schematic representation can be found in [9, figure 1]. W7-X contains 10 TDUs, with one lower and one upper TDU in each module, i.e. there are 5 lower TDUs (labeled 1l to 5l) and 5 upper TDUs (labeled 1u to 5u), see e.g. [5, 14] for a schematic representation. 18 PSI target elements were used for erosion/deposition studies, see figure 1 for a schematic representation of the locations and table 2 for tabulated positions together with an overview of applied analytical methods. Horizontal target position TM2h6 was used in all TDUs for monitoring

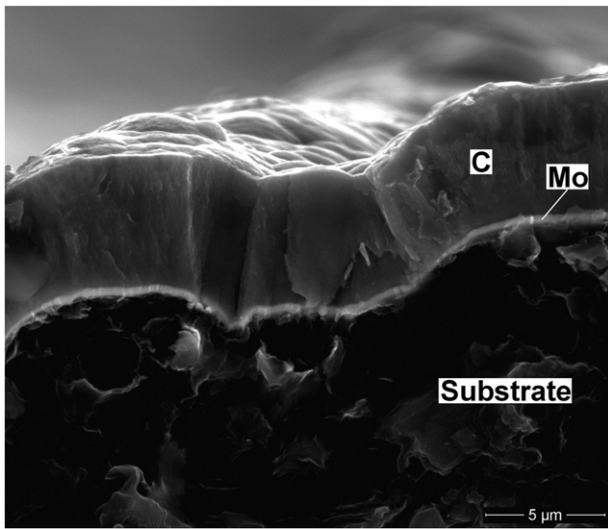


Figure 2. Scanning electron microscopy image of the fracture surface of the C/Mo marker coating before plasma exposure, showing the carbon marker coating (C), the Mo interlayer, and the fine-grain carbon substrate.

the toroidal asymmetry of the erosion/deposition distribution, additionally TDUs 5l and 5u contained PSI targets at positions TM1v5 and TM2v2 in the vertical and positions TM1h3 and TM3h6 in the horizontal targets.

2.3. Erosion/deposition marker layers

Erosion of carbon and deposition of eroded wall materials and impurities on the TDU, such as B, C, O, Ni, Fe etc, were determined by using marker layers of 5–10 μm thick carbon layers on top of 200–300 nm molybdenum, which were deposited on the fine grain graphite tiles of the PSI target elements. The Mo interlayer distinguishes the C marker layer from the bulk carbon of the tile for depth-profiling methods. Both layers were deposited using the CMSII technique [20], see figure 2 for an SEM image of the fracture surface of the coatings before plasma exposure.

Elastic backscattering spectrometry (EBS) was used at the IPP tandem accelerator [21] for quantitative analysis of the marker layers before and after exposure in W7-X applying 2.5 MeV incident protons at a backscattering angle of 165° and normal incidence. Typical EBS raw spectra are shown in figures 1 and 2 in [22]. A passivated implanted planar silicon (PIPS) detector having a nominal energy resolution of about 12 keV and a thickness of 300 μm was used. Pre-exposure measurements were made using a step width of 20 mm in poloidal direction, a smaller step width of 5 mm was used after exposure. About 3000 backscattering spectra were recorded.

The experimental spectra were analyzed with the simulation software SIMNRA [23, 24]. Cross-sections for non-Rutherford scattering from ^{12}C , ^{13}C and ^{16}O [25] were taken from SigmaCalc, and SRIM [26] stopping powers were used. Surface roughness was included in the analysis using the model described in [27].

The large number of experimental spectra rendered a manual analysis impossible. The spectra were therefore evaluated using the following methods:

- About 500 spectra from pre-exposure measurements were fitted using automated fits.
- Two different artificial neural networks (ANNs) were trained [28]. The model ANN 2 consisted of a carbon substrate and two layers: a Mo interlayer and a top carbon layer. Both layers could include roughness. Model ANN 3 had three layers: the Mo interlayer, the top carbon layer, and a mixed carbon/oxygen layer on top. The Mo interlayer and the carbon layer could include roughness.

Output parameters of the ANNs were the layer thicknesses and roughnesses of the marker layers and the spectra calibration parameters gain and offset. Charges were normalized previously. After training the ANNs evaluated a given spectrum in less than 1 s.

Layers deposited in OP 1.2b typically contained small amounts of boron originating from the boronizations, with the boron content typically below 10 at.%. Because boron and carbon could hardly be distinguished in the spectra, the ANNs were not trained for separating boron and carbon. Given numbers for deposited carbon are therefore always a carbon-rich mixture of carbon and boron, with the C/B ratio typically exceeding ten.

A FEI Helios Nanolab 600 was used for scanning electron microscopy (SEM) investigations. Cross-sections were obtained using a focused ion beam (FIB), energy-dispersive x-ray spectroscopy (EDX) was used for recording the lateral distribution of elements on the micro-scale. 5 keV was used as incident electron beam energy.

Surface roughness measurements were made with the optical three-dimensional profiler Olympus LEXT 3D Measurement Laser Microscope OLS4000 at a wavelength of 400–420 nm using a $100\times$ objective with a numerical aperture of 95%, resulting in an optical resolution of about 430 nm. The step widths in x - and y -direction were 0.625 μm .

3. Results

3.1. Surface morphology

Tiles at identical positions in different TDUs showed a very similar optical impression. Photos of the marker tiles at position TM2h6, see figure 1, in TDU 2u after the operational period OP 1.2b are shown in figure 3 top. Scanning electron micrographs (recorded using secondary electrons) of the surfaces at positions A–H are shown in figure 3 bottom, focused ion beam (FIB) cross-sections from positions A–H are shown in figure 4. The surfaces on tiles 024, E004 and partly on A004 showed only minor modifications by the plasma and the SEM image from position H can be taken as typical representation of the original structure of the marker layers. The initial surfaces are rough on a coarser scale due to the grinding process of the tiles, which results in linear grooves, and show larger hemispherical structures due to the coating process. The fine-grain graphite substrate material shows large pores, which

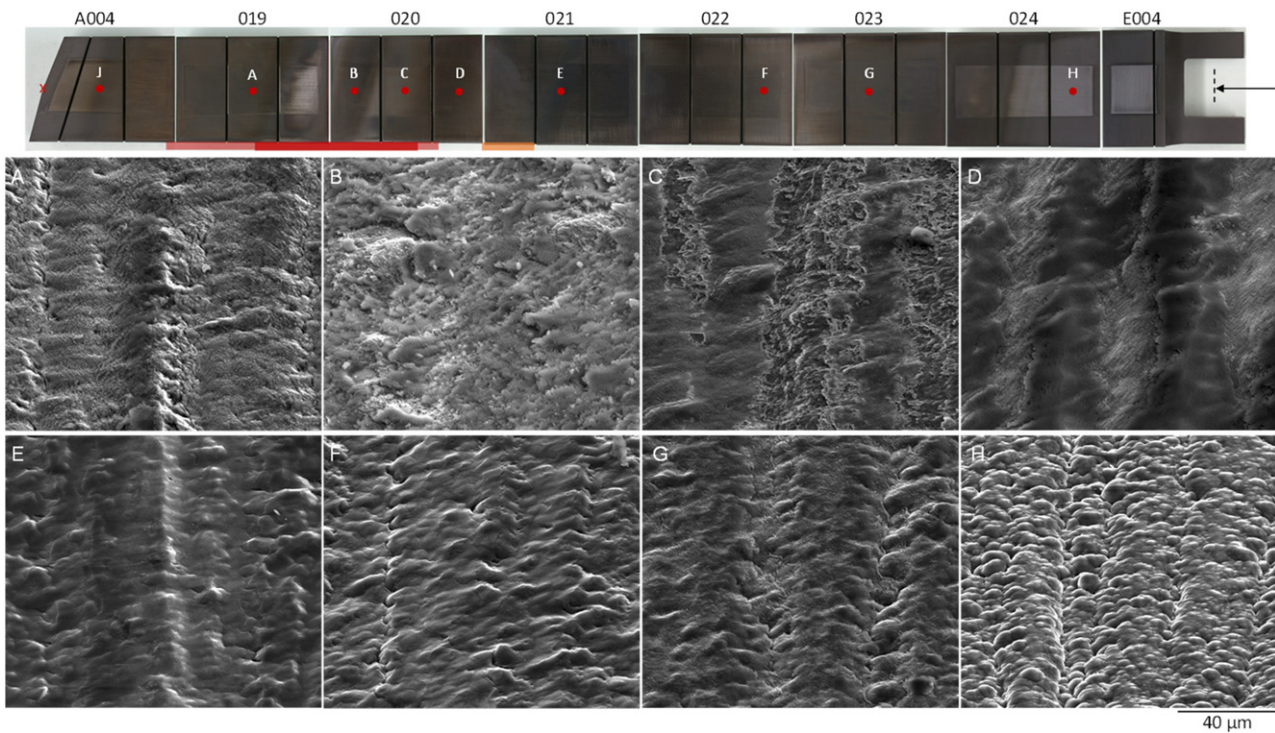


Figure 3. Top: target element TM2h6 from TDU 2u after the operational period OP 1.2b. The target element consists of tiles A004, 019 to 024, and E004. The width of target elements 019–024 is 75 mm each. The red x at the left side of tile A004 marks the origin for the coordinate system used for IBA measurements. Red dots labeled A–H indicate positions where scanning electron micrographs are shown below and FIB cross-sections are shown in figure 4. The dashed line on the right-hand side indicates the direction of the FIB cross-sections shown in figure 4, the arrow is the viewing direction. Roughness inclination angle distributions from positions C and J are shown in figures 6 and 7. The light red area below tiles 019 and 020 indicates the strike line area with net erosion, the dark red area indicates the area with highest erosion. The orange area below tile 021 is an area with stronger net deposition. Bottom: scanning electron micrographs from points A–H. Secondary electrons, tilt angle 52°.

are typical for this type of material. The Mo interlayer with a thickness in the range of 200–300 nm follows the surface structure of the substrate and is consequently quite rough, and also the carbon marker layer follows approximately the substrate structure.

Pos. A in figures 3 and 4 is an area with low erosion. The hilltop has been somewhat eroded, while the whole surface exhibits a small-scale roughening. Pos. B and C are areas of high erosion. Here the carbon marker layer has been fully eroded at hilltops and at plasma-inclined surfaces and the Mo interlayer is at the surface, see the red marked areas. In valleys and on plasma-averted hill sides the carbon layer is still present, but is partly eroded. The surface shows a small-scale roughening. However, despite this erosion-initiated small-scale roughness the overall roughness of these erosion-dominated areas is smaller than the roughness of the initial surfaces: the grinding grooves and hills have (more or less) disappeared as well as the initial hemispherical structures (see Pos. H for comparison). Pos. D is between the erosion-dominated areas B and C and the net deposition area on tile 21. Here the valleys exhibit a smoother impression and probably contain thin deposits, while hilltops and plasma-inclined faces show the typical microstructure of erosion areas. Positions E to G show thin deposits with thicknesses below 500 nm, see also figure 5. Deposits have a visually smoother

appearance than erosion-dominated areas. At the hilltops some small erosion might have occurred, but this is difficult to judge due to the thickness inhomogeneities of the initial layers. Tiles 024 and E004 show only minor modifications by the plasma, see above. Delaminations (of the C marker layer or of the Mo layer) were not found at any place.

3.2. Surface roughness

The surface morphology was recorded with an optical profiler at position J, see figure 3 top, where only minor modifications of the initial surface were observed, and at the high erosion position C using a lateral step width of 0.625 μm in toroidal and poloidal directions. The height profiles consisted of two-dimensional height maps with about 4700×4700 pixels, covering areas of approximately $3 \times 3 \text{ mm}^2$.

The surface roughness was characterized by the arithmetic mean roughness (sometimes called arithmetic mean deviation) S_A on 4 areas of $232 \times 232 \mu\text{m}^2$ each. These smaller areas allowed a more precise fit of the base profile using planes, the S_A values of the four different areas were averaged. The S_A value at position J was 2.18 μm , and 0.95 μm at position C. This decrease of the arithmetic mean roughness demonstrates the smoothing effect of the plasma exposure, as can be seen already qualitatively by comparing the visual impression of positions C and H in figures 3 and 4.

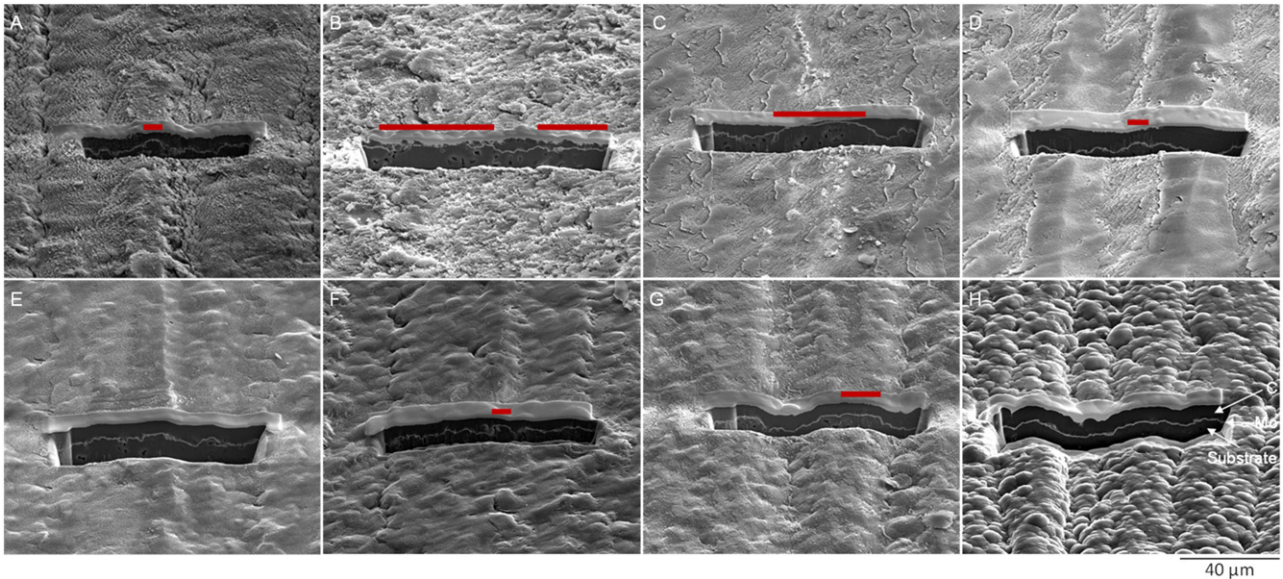


Figure 4. FIB cross-sections from positions A–H, see figure 3 for the positions and typical scanning electron micrographs of the surfaces. The surface area of the cross-section has been coated with a thin Pt layer before cross-sectioning, this layer is visible above the cross-section. The initial layer structure consisting of a 5–10 μm thick carbon layer on a thin Mo interlayer on the graphite substrate is labeled in subfigure H. Areas with potential erosion of the initial carbon marker layer are marked in red. Secondary electrons, tilt angle 52° .

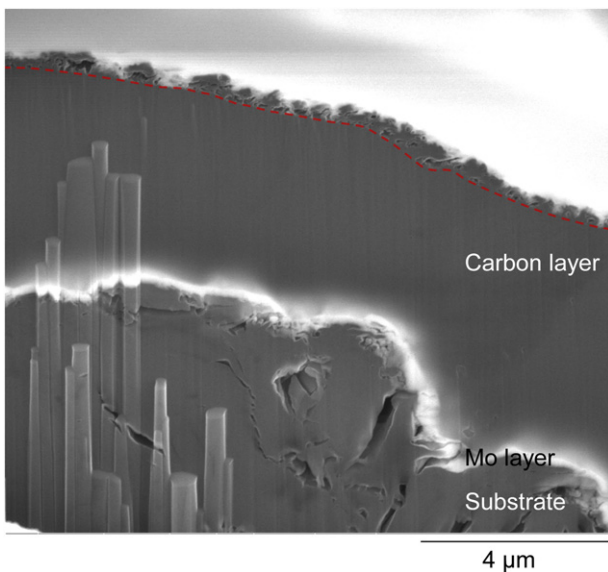


Figure 5. High resolution image of thin deposits at position G, see figure 3. The columnar structure in the lower left area of the cross-section is an artefact of the FIB cutting process. The initial surface is marked by the dashed red line, the material above has been deposited during plasma exposure. Secondary electrons, tilt angle 38° .

The arithmetic mean roughness provides only a crude characterization of the roughness. Therefore the local inclination angles φ_i of linear line profiles were determined from

$$\varphi_i = \arctan\left(\frac{z_{i+1} - z_i}{x_{i+1} - x_i}\right),$$

with z_i and z_{i+1} being the heights at positions i and $i + 1$, respectively, and x_i , x_{i+1} being the lateral coordinates at positions i and $i + 1$. Due to the surface structures (linear grooves

and hills) introduced by the grinding process the distributions of inclination angles were determined in poloidal and toroidal directions separately. The grinding direction was parallel to the poloidal direction, i.e., roughly perpendicular to the magnetic field lines.

The frequency distributions of the local inclination angles φ_i at positions J and C, see figure 3 top, are shown in figure 6. The distributions at position J are relatively broad, thus reflecting the relatively large roughness of the initial marker surface, see position H in figures 3 and 4. The direction parallel to the grinding is marked by a slightly narrower inclination angle distribution than for the direction perpendicular to the grinding grooves. The high-erosion position C is characterized by considerably narrower distributions both in poloidal and toroidal directions: this demonstrates the polishing effect of plasma erosion/deposition. The grinding direction still has a slightly narrower distribution than the direction perpendicular to the grinding grooves, but this difference is considerably smaller than at position J. This is a quantitative measure of the visual impression at position C in figures 3 and 4, that the grinding grooves are less pronounced after plasma exposure in high-erosion areas.

As described in [29] the two-dimensional height profiles were also subdivided in triangles formed by the regular mesh of measured data points and the inclination angles φ_i of their (local) surface normals towards the nominal surface normal were determined. The frequency distributions from positions J and C are shown in figure 7. The initial distribution at J is relatively wide with a broad maximum at an inclination angle around 26° . The distribution at the high erosion position C is considerably narrower with a maximum at about 15° . The mean inclination angle at position J is 38.4° compared to 23.9° at the high erosion position C. Again, this demonstrates the polishing effect of plasma erosion/deposition, resulting in

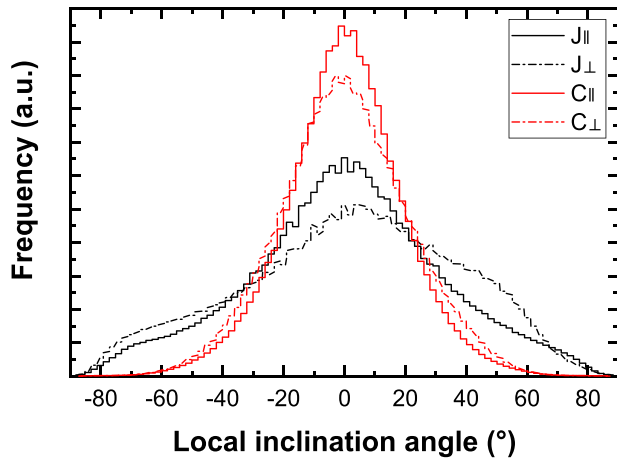


Figure 6. Frequency distribution of local inclination angles at positions J and C, see figure 3 top. || is parallel to the grinding direction in poloidal direction, \perp is perpendicular to the grinding direction in toroidal direction. Bin width 2° .

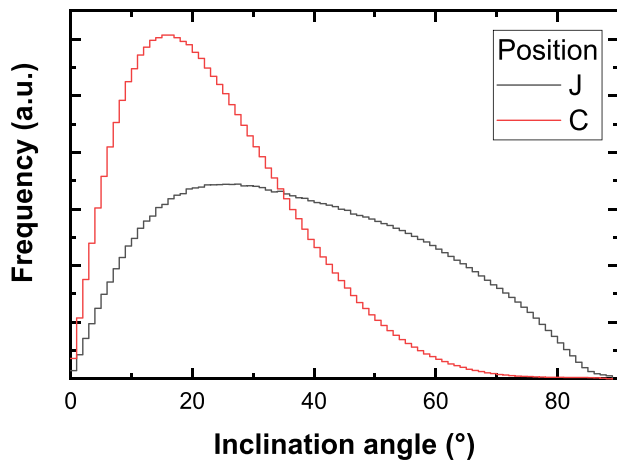


Figure 7. Frequency distribution of local planar inclination angles with respect to the nominal surface normal at positions J and C, see figure 3 top. Bin width 1° .

smoother surfaces with smaller inclination angles after plasma exposure. It should be noted that inclination angle distributions from line profiles, as shown in figure 6, and inclination angle distributions from triangular planes, as shown in figure 7, are just different views, i.e., one-dimensional versus two-dimensional height profiles, onto the same roughness.

It has been already shown experimentally and by computer simulations that the physical sputtering yield of a rough surface can deviate significantly from a smooth surface [30–34]: at normal incidence the sputtering yield of a (moderately) rough surface is typically higher than that of a smooth surface, while at grazing angles of incidence the physical sputtering yield of a rough surface is lower than that of a smooth surface. It has been already pointed out in [29] that ‘the governing parameter for description of the sputtering behaviour is the mean value of the surface inclination angle distribution, rather than the commonly used root mean square roughness’. In a fusion device with a magnetically confined plasma and grazing angles $>85^\circ$ of the magnetic field towards the surface

normal, ions typically hit material surfaces at grazing angles of incidence of 60° – 75° to the surface normal [35–37]. The observed plasma polishing effect of initially rough surfaces by erosion/deposition processes and the observed narrowing of the distribution of inclination angles therefore changes the erosion/deposition balance of the surfaces with incident plasma fluence. A decrease of the surface roughness typically results in an increased physical sputtering yield, especially for incident heavier ions such as boron, carbon or oxygen [38]. The observed plasma smoothing effect with increasing fluence is therefore expected to increase the erosion yield at the plasma strike line with increasing exposure time.

3.3. Erosion/deposition pattern

3.3.1. Horizontal target modules. The pre-exposure thicknesses of the Mo and C marker layers on target element TM2h6 in TDU 51 are shown in figure 8 as hollow symbols. The thicknesses were determined by EBS. A schematic view of the target element is shown at the very top. The origin of the coordinate system is the small tip in the middle of the element towards the pumping gap, see the red x in figure 3 top⁷. Pre-analysis layer thicknesses derived from the two different ANN analyses and the automatic fits show very good agreement. Initial thicknesses of the Mo and C layers show some scatter from tile to tile. This is caused by different positions of individual tiles in the coating device and the application of different coating runs. Some tiles showed some layer thickness gradient over the length of the tile, the maximum difference on individual tiles was of the order of 10%. This variation of layer thickness from tile to tile shows the necessity of pre-analysis of every tile.

The thicknesses of the molybdenum and carbon marker layers after exposure during OP 1.2b, as determined by the ANN 3 analysis, are shown in figure 8 as solid symbols. The carbon marker layer thickness after exposure is thinner than before exposure from about 100 nm to 220 nm, i.e., in this region the carbon layer has been partly eroded. At the position with maximum erosion around 150 nm, about 10^{19} C-atoms/cm² (about 1 μm) still remain, while the Mo layer below has the same thickness as initially. At around 80 nm and between 220 and 280 nm the amount of carbon is higher than initially, i.e., this is a net deposition area. At around 350 nm another small net erosion area can be observed.

Deposits consist mostly of carbon, but usually also contain some boron. While the boron signal can sometimes be qualitatively identified, a quantification is difficult due to the overlap of the B and C signals in the EBS spectra. As was shown in [10] the boron content in deposited layers is typically below 5 at.%. The term ‘carbon’ in this paper therefore refers to a carbon-rich mixture of boron and carbon. Oxygen is typically also visible at levels of a few at.%. Due to the porosity of deposited layers [10] it is generally difficult to distinguish if oxygen was incorporated into the layers during plasma operation or

⁷ Reference [9] used the gap between the first two tiles as origin for the coordinate system. For TM2h6 this is shifted by 64.7 mm compared to the present work and has a different prefix. The coordinate system in the present work has been made consistent with other diagnostics.

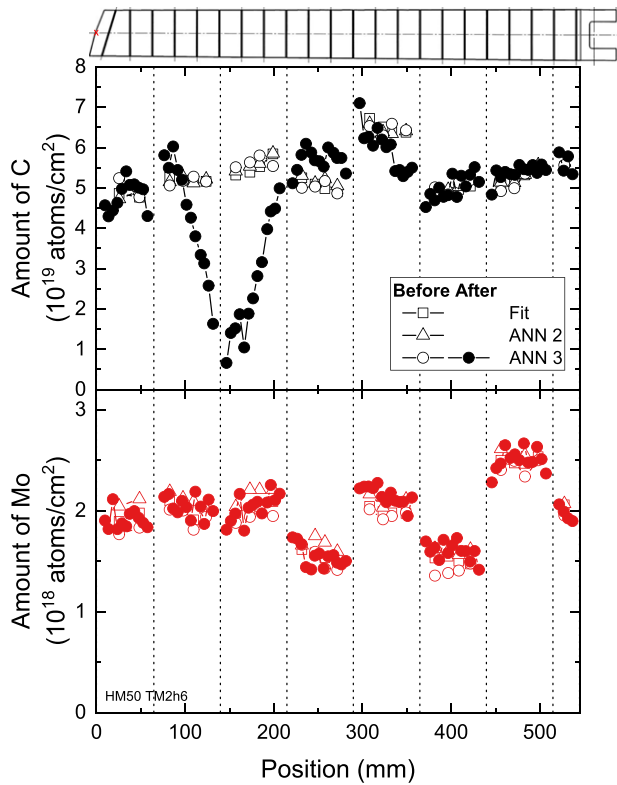


Figure 8. Thicknesses of the marker layers before exposure (hollow symbols) and after exposure (solid symbols) in OP 1.2b. Top: carbon; bottom: molybdenum; circles: thicknesses by the Artificial Neural Network analysis with 3 layers (ANN 3); triangles: thicknesses by the Artificial Neural Network analysis with 2 layers (ANN 2); squares: thicknesses from an automated fit. Very top: schematic representation of the target element, dashed lines are tile boundaries. The pumping gap, see figure 1, is on the left-hand side. The small red cross marks the scale origin. TDU 51 TM2h6.

during air exposure. Oxygen therefore will be not discussed here. As was already shown using laser-induced breakdown spectroscopy (LIBS), deposited layers typically also contain hydrogen [39–41]. This was not detectable with the applied analysis methods.

The differences of layer thicknesses before and after exposure during OP 1.2b, i.e., the net amounts of erosion of C and Mo, are shown in figure 9 for TDU 51 target element TM2h6. The shown pre-exposure layer thicknesses (figure 8) were linearly interpolated between the existing data points and (if necessary) extrapolated towards the tile edges. The highest erosion of about 5×10^{19} C-atoms/cm² is at the strike line around 150 mm, while a second net erosion area with a maximum erosion of about 1×10^{19} C-atoms/cm² is observed at around 350 mm. Net carbon deposition areas are observed at both sides of the strike line area at about 80 mm and 250 mm. The area towards the baffle >400 mm shows almost no changes. The thickness of the Mo-layer below the carbon layer is identical to its initial thickness, i.e., it has been not eroded and there were also no larger scale delaminations.

For some target elements the erosion of the carbon marker layer was small enough such that some carbon of the layer was still present and the underlying Mo interlayer has not been eroded (like in figures 8 and 9). However, on some other target

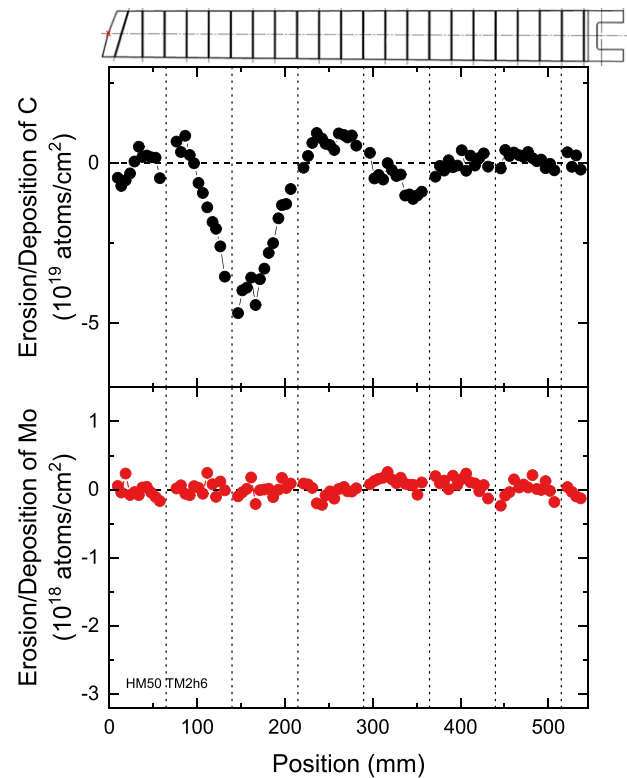


Figure 9. Net erosion of the marker layers during the discharge period OP 1.2b based on the Artificial Neural Network analysis ANN 3. Top: carbon; bottom: molybdenum. Deposition has positive, erosion has negative sign. Very top: schematic representation of the target element, dashed lines are tile boundaries. The pumping gap, see figure 1, is on the left-hand side. The small red cross marks the scale origin. TDU 51 TM2h6.

elements either the erosion was higher or the initial carbon layer thickness was thinner, so that at the strike line position the carbon marker was fully eroded and the underlying Mo layer got partly eroded. An example is shown in figure 10. In these cases of total erosion of the carbon marker layer, only a lower bound for the net carbon erosion during the campaign can be directly extracted from the measurements. However, a more realistic value can be obtained by the assumption that the invisible carbon erosion (i.e., the carbon erosion exceeding the erosion of the marker layer) is proportional to the Mo erosion. The proportionality factor was determined in areas where both carbon and molybdenum erosion occurred, which is possible due to the laterally inhomogeneous erosion on the microscale. The extrapolated net carbon erosion based on the Mo erosion is shown in figure 10 as dash-dotted line. This extrapolation introduces large uncertainties, because carbon and molybdenum erosion can have different origins: carbon is potentially removed by physical sputtering and by chemical erosion by H or O, while Mo can be only eroded by physical sputtering by heavier plasma impurities. An uncertainty of 33% is assumed for this extrapolation and shown as light grey areas in figure 10 (and the following figures).

The erosion pattern on target element TM2h6 in TDU 2u (figure 10) is qualitatively very similar to that on TDU 51 shown in figures 8 and 9: high carbon erosion is observed at

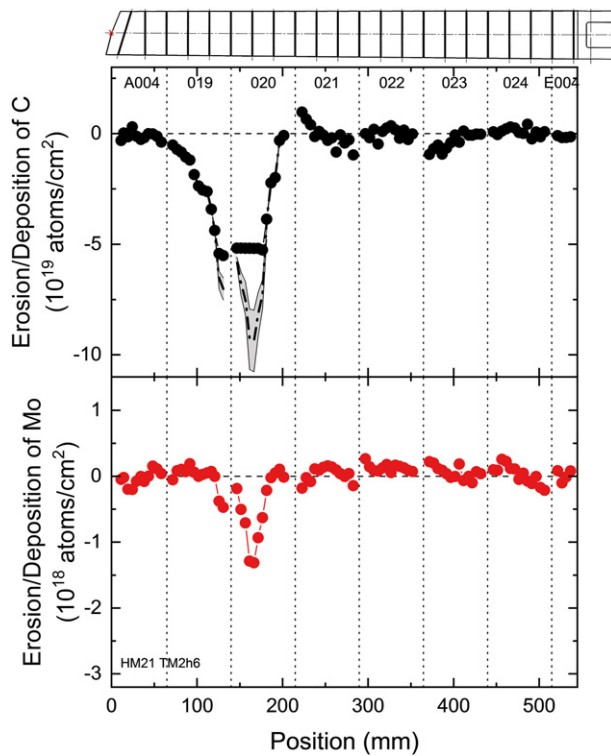


Figure 10. Net erosion of the marker layers during the discharge period OP 1.2b based on the Artificial Neural Network analysis ANN 3. Top: carbon; bottom: molybdenum. Deposition has positive, erosion has negative sign. Very top: schematic representation of the target element, dashed lines are tile boundaries. The pumping gap, see figure 1, is on the left-hand side. TDU 2u TM2h6, see figure 3. Numbers at the top are tile numbers. Dash-dotted line: extrapolated carbon erosion based on the erosion of the Mo layer; grey area: uncertainty of the extrapolation. The small red cross marks the scale origin.

the strike line from about 80–200 mm. On the right-hand side at about 250 mm adjacent to the strike line some deposition of carbon is observed. A second strike line with erosion is observed from about 370–400 mm.

The described erosion/deposition pattern is observed on all 10 TDUs on target element TM2h6: high carbon erosion is observed at the strike line from about 80–200 mm. On the left-hand side at about 70 mm adjacent to the strike line on some TDUs and on the right-hand side at about 250 mm adjacent to the strike line on all TDUs some deposition of carbon is observed. A second strike line with erosion is observed from about 320–370 mm. As can be seen in SEM images, the remaining area of the target elements shows thin deposits with thicknesses below the detection limit of EBS, i.e., the thickness of these deposits is below 500 nm. Hilltops in these areas may be somewhat eroded at some places.

The maximum erosion of carbon at the strike line position on target element TM2h6 was 10.8×10^{19} C-atoms/cm² (about 12 μ m). This was observed in TDU 2u and converts to a maximum erosion rate of 2.2×10^{16} C-atoms/(cm² s) (about 2.5 nm s⁻¹). The lowest erosion of carbon at the strike line position on target element TM2h6 was observed in TDU 5l and

Table 3. Peak net carbon erosion for the whole campaign and peak net carbon erosion rate at the strike line of the standard configuration. The lowest and highest observed values are given.

	OP 1.2a	OP 1.2b
Total net erosion (μ m)	14.5–20.8	5.2–12.0
Net erosion rate (nm s ⁻¹)	5.8–8.4	1.1–2.5

was 4.7×10^{19} C-atoms/cm², converting to an erosion rate of 9.8×10^{15} C-atoms/(cm² s) (about 1.1 nm s⁻¹), see table 3.

Target element 5l TM1h3 showed no erosion at the strike line position but small deposition around 200 mm: this is consistent with the finding that the erosion on TDU 5l was generally lower than in most other TDUs, probably due to a slight misalignment of this TDU. Target element 5u TM1h3 showed a very similar erosion pattern as target elements TM2h6 with substantial erosion at the strike line. Target elements 5l TM3h6 and 5u TM3h6 also showed a very similar erosion pattern as target elements TM2h6 with smaller erosion in 5l and substantial erosion in 5u at the strike line with a maximum erosion of 1.1×10^{20} C-atoms/cm² (about 12 μ m). This was also the highest measured erosion at the standard strike line position of all marker tiles and converts to a maximum observed carbon erosion rate of 2.3×10^{16} C-atoms/(cm² s) (about 2.5 nm s⁻¹).

Marker layers for erosion/deposition measurements were only available in target modules TM1h to TM3h. Some data about material deposition in target module TM4h can be found in [42].

The qualitative shape of the erosion pattern after OP 1.2b is comparable to the erosion pattern observed after OP 1.2a [9], except that the total erosion during OP 1.2b was smaller than during OP 1.2a. This will be discussed in more detail in section 3.4.

3.3.2. Vertical target modules. The erosion/deposition pattern on the vertical target elements TM1v5 and TM2v2, see figure 1, were qualitatively very similar to the pattern on the horizontal elements. TM2v2 in TDU 5l (figure 11) and 5u (figure 12) showed erosion at the strike line position around 150 mm and some carbon deposits towards the pumping gap at about 80 mm. Small erosion was observed close to the pumping gap and towards the inner wall. The erosion at the strike line of TDU 5l TM2v2, see figure 11, was higher than the initial carbon marker layer thickness, so that also the Mo interlayer was partly eroded. The most probable carbon erosion was extrapolated from the combined carbon and Mo erosion (dash-dotted line in figure 11) together with the uncertainty of this extrapolation (light grey are in figure 11). See section 3.2.1 for details. The erosion pattern on TDU 5u TM2v2 was considerably broader, but with a smaller maximum erosion, so that some fraction of the top carbon marker layer still was present and the underlying Mo interlayer has not been eroded.

Target elements TM1v5 in TDUs 5l and 5u showed no carbon erosion but thin deposits. Marker layers for erosion/deposition measurements were only available in target modules TM1v and TM2v. Some data about material deposition in target module TM3v can be found in [42].

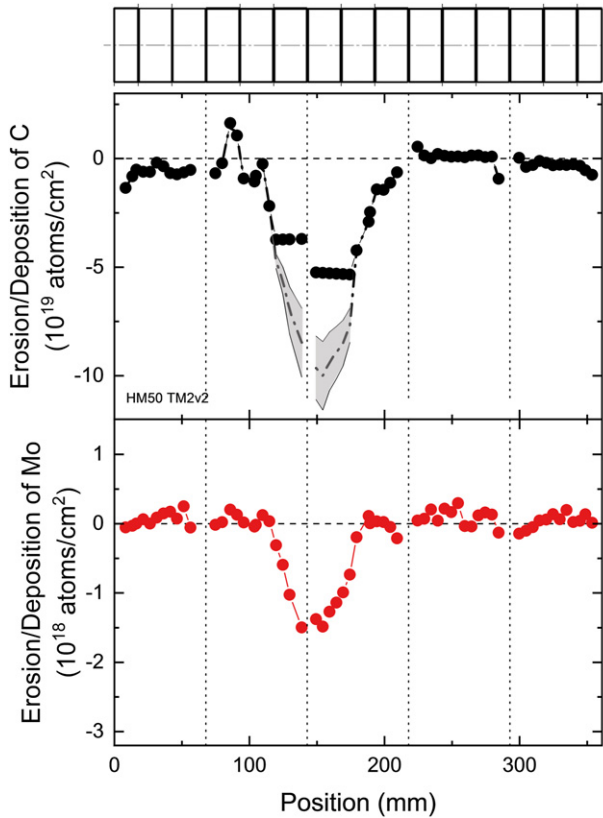


Figure 11. Net erosion of the marker layers during the discharge period OP 1.2b based on the Artificial Neural Network analysis ANN 3. Top: carbon; bottom: molybdenum. Deposition has positive, erosion has negative sign. Very top: schematic representation of the target element, dashed lines are tile boundaries. The pumping gap, see figure 1, is on the left-hand side. TDU 51 TM2v2, see figure 1. Dash-dotted line: extrapolated carbon erosion based on the erosion of the Mo layer; grey area: uncertainty of the extrapolation.

3.4. Integral carbon erosion

Carbon erosion in the different modules is shown in figure 13 for both operational periods OP 1.2a [9] and OP 1.2b. The erosion/deposition pattern was integrated along the middle of target element TM2h6. Dark grey bars are the directly measured C erosion. This can, however, underestimate the real erosion during the whole campaign due to the complete removal of the carbon marker layer at the strike line, see figures 10 and 11. The light grey bars show the extrapolated carbon erosion based on the observed Mo erosion, see figures 10 and 11. The uncertainty of this extrapolation from Mo erosion to C erosion (light grey areas in figures 10 and 11) is indicated by the error bars. Note the different y-scales in figure 13 left and right by a factor of about two. The carbon erosion on TDU 11 could not be determined during OP 1.2b due to the use of W-coated marker layers in this TDU [43].

The main difference between OP 1.2a and OP 1.2b is the considerably higher net erosion in OP 1.2a compared to OP 1.2b, see figure 13. The qualitative erosion pattern, however, is relatively similar in OP 1.2a and OP 1.2b: both TDUs in module two showed the highest erosion, and TDU 51 had the lowest erosion in both operational periods. The maximum difference of carbon erosion between the highest value (in 2u) and

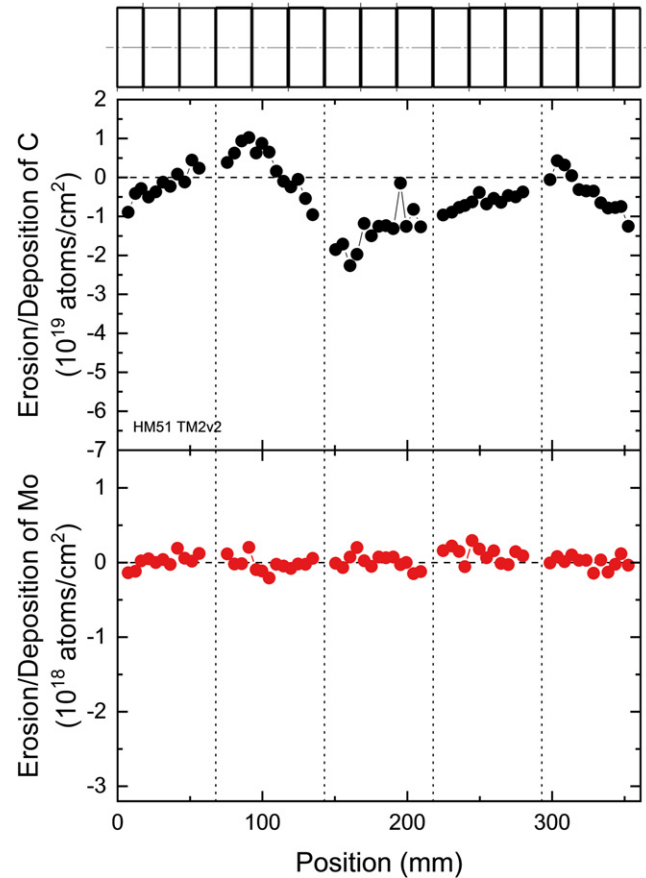


Figure 12. Net erosion of the marker layers during the discharge period OP 1.2b based on the Artificial Neural Network analysis ANN 3. Top: carbon; bottom: molybdenum. Deposition has positive, erosion has negative sign. Very top: schematic representation of the target element, dashed lines are tile boundaries. The pumping gap, see figure 1, is on the left-hand side. TDU 5u TM2v2, see figure 1.

the smallest value (in 5l) is within a factor of about two in both periods. Asymmetries in power fluxes were already observed by thermographic measurements [14] and are probably due to mechanical misalignments of TDUs with respect to the magnetic field. Qualitative similarities between OP 1.2a and OP 1.2b are therefore expected, as the alignment of the TDUs was not changed between these two operational phases.

The energy deposition on different TDU modules was determined by the temperature rise of thermocouples (TCs) attached to the rear sides of the modules, see figure 12 in [44]. The energy deposition (with applied symmetrized trim coil currents) is correlated with the erosion pattern: the TCs showed higher temperature rises for TDUs 2u and 5u and lower temperature rises for TDUs 1l, 4u, 5l. This agrees with the observed erosion pattern, see figure 13, with higher erosion in 2u and 5u and smaller erosion in 1l, 4u, 5l. In TDUs 3l and 3u the temperature rise of the TCs was small: this is reflected in the smaller erosion during OP 1.2b, but not in OP 1.2a. Such differences might be caused by the fact, that the TC temperature rise was determined in individual discharges, while the net erosion is an integration over the whole campaign with many different discharges. Furthermore, the TC temperature rise is proportional to the deposited energy during a discharge, which,

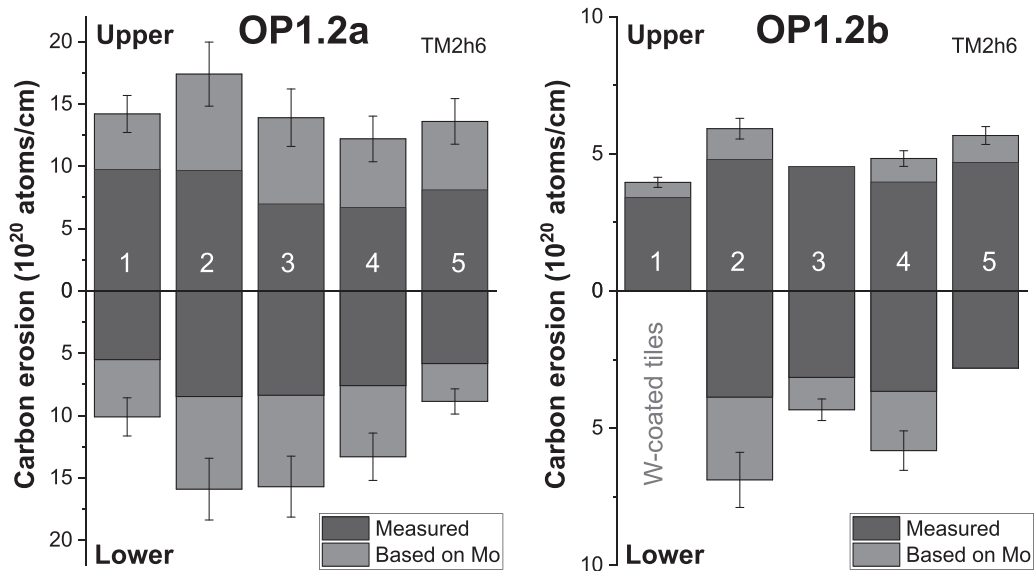


Figure 13. Integrated erosion of carbon from the marker layers in the upper and the lower TDUs. Integration along the center of target element TM2h6. Dark grey bars: directly measured carbon erosion; light grey bars: carbon erosion extrapolated based on the erosion of Mo, see figure 10. Uncertainties see figure 10. Left: operational period OP 1.2a; right: operational period OP 1.2b. Note the different y-scales of the left and right figures. During OP 1.2b the carbon erosion on TDU 11 could not be determined due to the use of W-coated marker layers there.

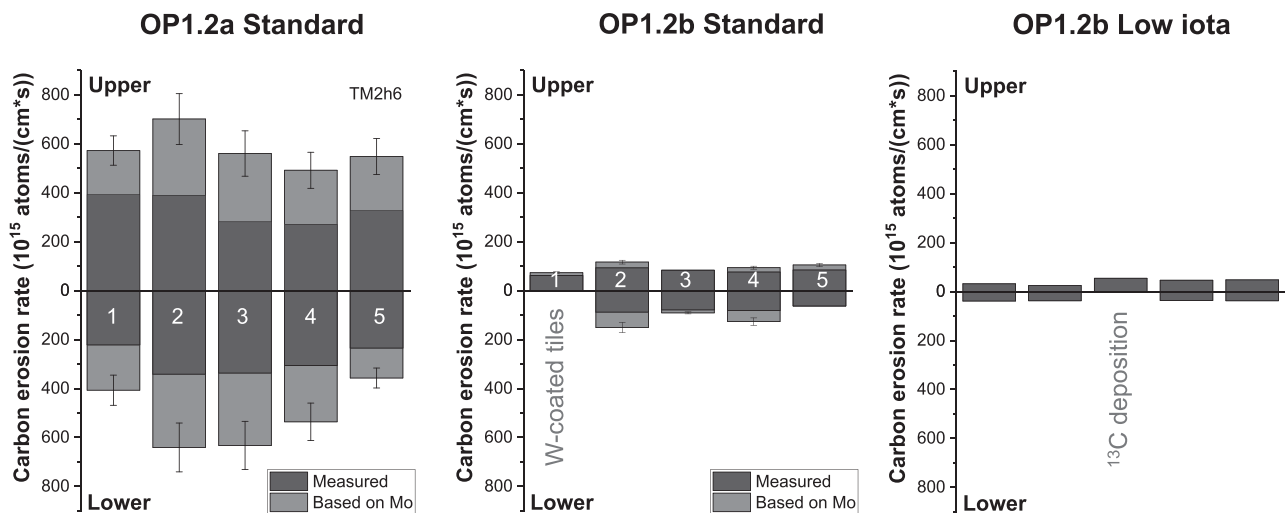


Figure 14. Integrated net carbon erosion rates of the marker layers in the upper and the lower TDUs. Integration along the center of target element TM2h6. Dark grey bars: directly measured carbon erosion rates; light grey bars: carbon erosion rates extrapolated based on the erosion of Mo, see figure 10. Uncertainties see figure 10. Left: operational period OP 1.2a standard configuration; middle: OP 1.2b standard configuration; right: OP 1.2b low iota configuration. The carbon erosion rate on TDU 11 could not be determined during OP 1.2b due to the use of W-coated marker layers in this TDU. The carbon erosion rate on TDU 31 in low iota configuration could not be determined due to the formation of thick ^{13}C layers by puffing of $^{13}\text{CH}_4$ at this location.

for identical plasma conditions, is proportional to the *gross* carbon erosion. However, the *net* carbon erosion depends also on carbon redeposition: this may vary in different TDUs due to local variations of divertor plasma parameters or impurity concentrations.

When comparing OP 1.2a and OP 1.2b, it should be kept in mind that the discharge time in OP 1.2b was about 2.5 times longer than in OP 1.2a. A direct comparison of the total erosion therefore makes only limited sense, and it is more reasonable to compare the erosion rates. These are shown in

figure 14. From OP 1.2a to OP 1.2b the net carbon erosion rate in standard configuration dropped by a factor of 5–6. The net carbon erosion rate in low iota configuration is lower as compared to the standard configuration by a factor of about 2. However, it should be kept in mind that the erosion at the strike line of the low iota configuration is a small net deposition area during standard configuration. The low erosion rate in low iota configuration therefore may be due to the fact that carbon eroded during low iota discharges is replaced by carbon deposited during standard discharges.

The erosion pattern varies from one target module to another in every TDU, and, as shown in figure 13, also shows variations between the different TDUs. The TC data in [44] indicate, that power fluxes in standard configuration are highest to horizontal target modules TM1h to TM5h (see figure 1), while the power flux to target modules TM6h and TM7h are considerably lower. For the determination of the total carbon erosion, we therefore only have to consider modules TM1h to TM5h in all 10 TDUs, i.e. in total 50 target modules. As shown by thermography, within each target module toroidal symmetry can be assumed. From the measured poloidal distribution of carbon erosion on 13 horizontal target elements this extrapolates to 13 horizontal target modules, assuming toroidal symmetry in each target module. For the remaining 37 horizontal target modules without erosion/deposition information the erosion has to be interpolated based on the TC data from [44], assuming proportionality between carbon erosion and temperature rise of the TCs. This results in 13.7 ± 2.3 g of net carbon erosion for all 10 horizontal targets, see table 1.

For the vertical targets a different extrapolation has to be performed, because TC data have not been published for the vertical targets. W7-X has 30 vertical target modules, and on only 4 of these vertical modules the erosion was determined in poloidal direction. An extrapolation to the vertical target is therefore only possible by assuming identical erosion on all 10 TDU vertical targets. On the basis of thermography it can be assumed that half of the length of TM1v (in toroidal direction) and half of the length of TM2v have full erosion, while half of the length of TM2v have 50% erosion. With these assumptions, a carbon erosion at the vertical targets of 6.7 ± 3.4 g can be derived. Here we assumed an uncertainty of 50% for the carbon erosion on the vertical targets due to the assumption of identical erosion in all 10 TDUs. The integral carbon erosion (horizontal and vertical targets for all 10 TDUs) was therefore 20.4 ± 5.7 g carbon during OP 1.2b, see table 1. This has to be compared to the total carbon erosion of 48 ± 14 g carbon during OP 1.2a, see table 1. The net carbon erosion rate in OP 1.2a was 13.9 ± 3.4 mg s⁻¹ at the horizontal target and 4.2 ± 1.8 mg s⁻¹ at the vertical target in OP 1.2a, which dropped to 2.3 ± 0.4 mg s⁻¹ at the horizontal target and 0.9 ± 0.5 mg s⁻¹ at the vertical target in OP 1.2b.

4. Discussion

Very high plasma concentrations of oxygen and carbon impurities were observed during the operational period OP 1.2a [10, 11] caused by outgassing of H₂O from graphite tiles [13]. Carbon was therefore removed from the TDU by physical and chemical erosion by hydrogen and oxygen ions and by physical sputtering by carbon ions. As already discussed in [9] the main erosion mechanism during OP 1.2a was chemical sputtering by oxygen due to formation of CO and (to a minor extent) CO₂ [45]. The ejected carbon atoms then could sputter further carbon atoms by physical sputtering. However, self-sputtering of carbon by carbon ions plays only a smaller role for net carbon erosion: because the reflection coefficient of incident carbon is small, sputtering yields above one are necessary for net erosion, while net deposition of carbon is obtained

for sputtering yields below about one. Carbon incidence therefore results under most plasma conditions in net deposition rather than erosion. Nevertheless, self-sputtering of carbon by carbon ions is important for maintaining the carbon impurity concentration in the plasma. The erosion yield of carbon by hydrogen ions is only 0.01–0.03 C/H-ion at temperatures in the range from room temperature to about 600 K, while only at elevated temperatures around 800 K the chemical erosion yield (by formation of CH₄) reaches higher values of about 0.1 C/H-ion [46].

Boronizations in OP 1.2b decreased the oxygen concentration in the plasma by 1–2 orders of magnitude [10, 11]. This decreased impurity concentration led to the described decrease of net carbon erosion at the TDU by a factor of 5–6. In OP 1.2b physical and chemical erosion of carbon by hydrogen and sputtering of carbon by carbon ions (and to a minor extend by other impurities like boron and oxygen) were probably the dominant erosion mechanisms. Sputtering by impurity ions probably also explains the observed erosion of the Mo layer at the strike line: the erosion yield of molybdenum by incident hydrogen-ions is very low and has a high threshold energy of 201 eV [47], so that hydrogen cannot be responsible for the observed erosion.

5. Conclusions

Net carbon erosion and deposition were determined during the operational phase OP 1.2b at the test divertor unit (TDU) of W7-X using 18 special PSI target elements. Target element TM2h6 was used in all TDUs, thus allowing us to determine inhomogeneities between different TDUs. The target elements contained coated marker layers of 5 to 10 μm carbon on top of about 300 nm molybdenum. Compositions and thicknesses of these layers were measured before and after exposure in W7-X by EBS with 2.5 MeV incident protons.

Carbon erosion was observed at the strike line of the standard configuration of all TDUs, a considerably smaller erosion was measured at the strike line of the low iota configuration. Some carbon deposition was observed left and right of the standard configuration strike line. In total 20.4 ± 5.7 g carbon were eroded during OP 1.2b from the TDU. The total net erosion on TDUs in different modules scattered within a factor of two between the TDU with the lowest and the highest erosion. The carbon erosion rate decreased by a factor of 5–6 compared to OP 1.2a due to boronizations: these decreased the oxygen concentrations considerably and resulted in a decrease of chemical erosion due to formation of CO. The resulting decreased impurity concentrations enabled enhanced plasma operation.

Eroded surfaces were measurably smoother than the initial material due to erosion/redeposition phenomena, which result in a higher erosion of hilltops and a filling of valleys with redeposited carbon. This smoothing effect results in a decrease of the arithmetic mean roughness and a decrease of the mean value of the microscopic inclination angle distribution, finally resulting in higher physical sputtering yields of plasma-exposed surfaces. This effect depends on particle fluence (or plasma exposure time): the plasma therefore creates

its own surface structures which can be quite different from the initial surfaces. This renders investigations and numerical simulations of erosion/deposition phenomena even more difficult.

The maximum erosion rate in OP 1.2b at the strike line of the Standard configuration was 1.1–2.5 nm s⁻¹, depending on TDU and position in the TDU. Assuming the same erosion rate for long-pulse discharges with anticipated pulse lengths up to 1800 s, this projects to a maximum erosion of 2–4.5 μm per long pulse at the strike line. For divertor tiles with thicknesses in the range of several mm erosion therefore limits the number of possible long-pulse discharges to the order of 1000. For high impurity concentrations, especially of oxygen, in the plasma, erosion increases, thus limiting the number of possible long-pulse discharges to a few hundred. However, the large amounts of eroded and redeposited carbon may result in the build-up of thick redeposited layers, which can flake off the substrate. This can severely impede plasma performance. Long-pulse operation therefore probably requires low oxygen concentrations. The reduction of the oxygen concentration by a boronization lasts for a few thousand plasma seconds [17], so that the execution of small numbers of long-pulse discharges seems feasible by the currently used boronizations. Even longer discharges or steady-state operation may require a continuous replenishment of boronization layers, for example by continuous boron injection [48]. However, a reduction of erosion by using either detached divertor conditions and/or a divertor material with lower erosion yield such as tungsten may be additionally required. Due to the very high tritium retention of carbon-based materials the use of tungsten may be inevitable for a future stellarator fusion reactor. First investigations on the use of tungsten in W7-X have already been performed [43], and a carbon-free device with a tungsten divertor is envisaged for the operational period OP 3 in the year 2031.

Acknowledgments

We gratefully acknowledge the technical assistance of J Dorner and M Fußeder from IPP Garching in all ion beam analysis measurements. Measurements using the optical profiler were made by K Hunger. This work has been carried out within the framework of the EUROfusion Consortium, funded by the European Union via the Euratom Research and Training Programme (Grant Agreement No. 101052200—EUROfusion). Views and opinions expressed are however those of the author(s) only and do not necessarily reflect those of the European Union or the European Commission. Neither the European Union nor the European Commission can be held responsible for them.

ORCID iDs

M. Mayer  <https://orcid.org/0000-0002-5337-6963>
 M. Balden  <https://orcid.org/0000-0002-8755-9370>
 S. Brezinsek  <https://orcid.org/0000-0002-7213-3326>

V.V. Burwitz  <https://orcid.org/0000-0002-9187-4867>
 C. Cupak  <https://orcid.org/0000-0003-4502-5749>
 P. Hired  <https://orcid.org/0000-0002-2119-8648>
 D. Naujoks  <https://orcid.org/0000-0003-4265-6078>
 C. Ruset  <https://orcid.org/0000-0002-7348-3686>
 T.F. Silva  <https://orcid.org/0000-0002-7643-2198>

References

- [1] Beidler C. et al 1990 *Fusion Technol.* **17** 148
- [2] Wolf R.C. et al 2017 *Nucl. Fusion* **57** 102020
- [3] Bosch H.-S. et al 2017 *Nucl. Fusion* **57** 116015
- [4] Sunn Pedersen T. et al 2017 *Phys. Plasmas* **24** 055503
- [5] Peacock A. et al 2009 *Fusion Eng. Des.* **84** 1475
- [6] Pedersen T. et al 2019 *Plasma Phys. Control. Fusion* **61** 014035
- [7] Pedersen T. et al 2016 *Nat. Commun.* **7** 13493
- [8] Hirsch M. et al 2008 *Plasma Phys. Controlled Fusion* **50** 053001
- [9] Mayer M. et al 2020 *Phys. Scr.* **T171** 014035
- [10] Sereda S. et al 2020 *Nucl. Fusion* **60** 086007
- [11] Wang E. et al 2020 *Phys. Scr.* **T171** 014040
- [12] Fuchert G. et al 2020 *Nucl. Fusion* **60** 036020
- [13] Brezinsek S. et al 2022 *Nucl. Fusion* **62** 016006
- [14] Gao Y., Jakubowski M.W., Drewelow P., Pisano F., Puig Sitjes A., Niemann H., Ali A. and Cannas B. (W7-X Team) 2019 *Nucl. Fusion* **59** 066007
- [15] Barbui T. et al 2018 *45th EPS Conf. Plasma Physics* (Prague, Czech Republic) vol P4 p 1018
- [16] Effenberg F. et al 2019 *Nucl. Mater. Energy* **18** 262
- [17] Gorjaev A. et al 2020 *Phys. Scr.* **T171** 014063
- [18] Dhard C.P. et al 2021 *Phys. Scr.* **96** 124059
- [19] Dhard C.P. et al 2017 *Phys. Scr.* **2017** 014010
- [20] Ruset C., Grigore E., Munteanu I., Maier H., Greuner H., Hopf C., Phylipps V. and Matthews G. 2009 *Fusion Eng. Des.* **84** 1662
- [21] Mayer M. et al 2020 *Nucl. Fusion* **60** 025001
- [22] Dhard C.P. et al 2019 *Fusion Eng. Des.* **146** 242
- [23] Mayer M. 1997 *SIMNRA User's Guide Technical Report IPP 9/113* Max-Planck-Institut für Plasmaphysik (Garching, Germany)
- [24] Mayer M. 2014 *Nucl. Instrum. Methods Phys. Res. B* **332** 176
- [25] Gurbich A.F. 2016 *Nucl. Instrum. Methods Phys. Res. B* **371** 27
- [26] Ziegler J.F. 2004 *Nucl. Instrum. Methods Phys. Res. B* **219–220** 1027
- [27] Mayer M. 2002 *Nucl. Instrum. Methods Phys. Res. B* **194** 177
- [28] Guimarães R.d.S. et al 2021 *Nucl. Instrum. Methods Phys. Res. B* **493** 28
- [29] Cupak C. et al 2021 *Appl. Surf. Sci.* **570** 151204
- [30] Küstner M., Eckstein W., Dose V. and Roth J. 1998 *Nucl. Instrum. Methods Phys. Res. B* **145** 320
- [31] Küstner M., Eckstein W., Hechtel E. and Roth J. 1999 *J. Nucl. Mater.* **265** 22
- [32] von Toussaint U., Mutzke A. and Manhard A. 2017 *Phys. Scr.* **T170** 014056
- [33] Arredondo R., Oberkofler M., Schwarz-Selinger T., von Toussaint U., Burwitz V.V., Mutzke A., Vassallo E. and Pedroni M. 2019 *Nucl. Mater. Energy* **18** 72
- [34] Kelemen M. et al 2021 *J. Nucl. Mater.* **555** 153135
- [35] Chodura R. 1982 *J. Nucl. Mater.* **111–112** 420
- [36] Khaziev R. and Curreli D. 2015 *Phys. Plasmas* **22** 043503
- [37] Abe S. et al 2021 *Phys. Scr.* **96** 124039
- [38] Mayer M., Kandler M., Dhard C.P., Elgeti S., Gao Y., Jakubowski M., Naujoks D. and Rudischhauser L.

- (W7-X Team) 2022 Assessment of carbon net erosion/deposition at the divertor of W7-X (Presented at PSI 2022, Submitted to Nuclear Materials and Energy)
- [39] Zhao D. *et al* 2020 *Phys. Scr.* **T171** 014018
- [40] Zhao D. *et al* 2021 *Nucl. Fusion* **61** 016025
- [41] Oelmann J. *et al* 2021 *Nucl. Mater. Energy* **26** 100943
- [42] Zhao M. 2022 Distributions of deposits and hydrogen on the upper and lower divertor target elements of Wendelstein 7-X (in preparation)
- [43] Mayer M. *et al* 2021 *Phys. Scr.* **96** 124070
- [44] Lazerson S.A. *et al* 2018 *Plasma Phys. Control. Fusion* **60** 124002
- [45] Winter J. 1996 *Plasma Phys. Control. Fusion* **38** 1503
- [46] Balden M. and Roth J. 2000 *J. Nucl. Mater.* **280** 39
- [47] Eckstein W. 2007 Sputtering yields *Sputtering by Particle Bombardment* (Topics in applied Physics vol 110) ed R. Behrisch and W. Eckstein (Berlin: Springer)
- [48] Bortolon A. *et al* 2020 *Nucl. Fusion* **60** 126010